

Processing, microstructure, and properties of ternary high-strength Cu–Cr–Ag in situ composites

D. Raabe^{a,*}, K. Miyake^b, H. Takahara^b

^a *Max-Planck-Institut für Eisenforschung, Max-Planck-Str. 1, 40237 Düsseldorf, Germany*

^b *Corporate Research and Development Center, Mitsui Kinzoku, 1333-2 Haraichi, Ageo-Shi, Saitama 362, Japan*

Received 6 December 1999; received in revised form 6 April 2000

Abstract

A new class of ternary in situ metal matrix composites (MMCs) with high strength and high electrical conductivity consisting of heavily co-deformed Cu, Cr, and Ag is introduced. Three alloys are investigated in detail, namely, Cu–10wt.%Cr–3wt.%Ag, Cu–10wt.%Cr–1wt.%Ag, and Cu–4.5wt.%Cr–3wt.%Ag. The alloys were produced by inductive melting and chill casting. Because Cu–Cr and Cu–Cr–Ag alloys with hypereutectic Cr content are less ductile than previously investigated Cu–Nb, Cu–Ag, and Cu–Nb–Ag alloys, special attention was placed on optimizing microstructure with respect to both strength and ductility using thermal and thermo-mechanical processing schemes. These included various combinations of swaging, heavy wire deformation (using different lubricants), solution annealing at different temperatures followed by quenching, and aging at different temperatures. Optimized processing allows one to attain maximum wire strains of $\eta = 8.48$ ($\eta = \ln(A_0/A)$, A : wire cross-section). The wires have very high strength (for instance Cu–10wt.%Cr–3wt.%Ag: 1260 MPa at a strain of $\eta = 8.48$) and good electrical conductivity (62% of the conductivity of pure Cu (IACS) at a strain of $\eta = 2.5$ after solution treatment). Up to wire strains of $\eta \approx 8.5$ the strength is equal to that of Cu–20wt.%Nb. The wire strength is much higher than predicted by the linear rule of mixtures. The investigation presents the evolution of microstructure during the various thermo-mechanical treatments and relates the results to the observed mechanical and electrical properties. The strength is discussed in terms of Hall–Petch-type hardening. © 2000 Elsevier Science S.A. All rights reserved.

Keywords: Ternary Cu-base composites; In situ MMC; Cu–Cr–Ag; High strength, High conductivity

1. Introduction

Heavily strained binary metal matrix composites (MMCs) consisting of Cu as matrix metal and a body centered cubic (bcc) transition metal with low solubility in Cu such as Nb [1–13] or Cr [14–16] as second phase have been the subject of extensive research over the last two decades. Further investigations along these lines were conducted on Cu-base MMCs using face centered cubic (fcc) Ag as a second metal [17–24].

Two reasons drive these efforts. The first reason is the need for alloys with very high strength and good electrical conductivity which can be used in highly mechanically stressed electrical devices. Prominent ex-

amples are in the areas of high field capacitor driven pulsed or steady-state, Bitter-type direct current magnet design, robotics, cables in aerospace applications, and electrical contacts [25–27]. The need for high strength materials in magnet design is due to the high Lorentz forces on the conductor during operation. High electrical conductivity is necessary in order to minimize joule heating occurring in resistive and pulse coils. Robotics and related electronics cables are often severely mechanically stressed, but their maximum electrical conductivity is usually less critical when compared to high-field magnet design. Electrical contacts must have low resistivity and high resistance to wear. The second reason for pursuing research in this field is that the unusual mechanical and electromagnetic properties observed and their dependence on microstructure have raised a number of fundamental questions. The most important among these topics is probably the extreme

* Corresponding author. Tel.: +49-211-6792278/340; fax: +49-211-6792333.

E-mail address: raabe@mpie.de (D. Raabe).

hardening behavior of Cu-base in situ composites which leads them surprisingly close to the theoretical limits of strength under uniaxial loads. Important aspects in that context are basic dislocation issues such as multiplication, glide, cell formation, and pile-up of dislocations in materials with an extremely high interface density; dislocation-interface issues such as the generation of secondary interface dislocation arrays, the complete penetration of thin metal fibers by lattice dislocations; and structural issues such as structural changes of the matrix and of the fiber material, the generation of structurally less ordered (glass-like) areas in the fibers, and the gradual formation of whiskers.

While much attention was devoted to the development and understanding of binary Cu-bcc [1–16] and Cu–Ag alloys [17–24], less efforts were made to widen the spectrum of in situ MMCs towards ternary Cu-base alloys. Some recent investigations aim at filling this gap. Morris and Joyce worked on hypereutectic Cu–2wt.%Cr–0.3wt.%Zr alloys [28], Verhoeven et al. on Cu–15wt.%Nb–2wt.%Ag alloys [7], Troxel on dispersoid-strengthened Cu–10wt.%Nb–(0.3 → 1.1)wt.%Al₂O₃ alloys [29], Fritzemeier on Cu–15wt.%Nb–2wt.%Ag alloys [30], Spitzig et al. on Cu–20wt.%Nb–7wt.%Ag alloys [31], Spaic and Pristavec on Cu–(1 → 7)wt.%Ag–0.3wt.%Zr alloys [32], and Raabe et al. on Cu–4wt.%Nb–8.2wt.%Ag alloys [33–37]. Taking a practical perspective, the development of ternary Cu-base composites usually follows two criteria. First, it aims at further improving the mechanical properties of conventional binary alloys without severely deteriorating their electromagnetic properties. A second aspect in moving from binary to ternary alloys lies in cost reduction. For instance, pure Nb or Ag are costly ingredients which impede the large scale application of such new materials for devices other than high field magnets. A useful strategy for meeting both goals lies in exploiting both filamentary Hall–Petch-type hardening and classical age hardening at the same time. Both effects are due to the interaction of mostly incoherent heterophase interfaces with lattice dislocations. This means that the physics of hardening in ternary alloys has essentially the same origin as in binary alloys. However, adding a third element allows one to exploit a larger variety of possible kinetic paths for attaining a certain flow stress–conductivity profile. In other words, the variation in possible thermo-mechanical treatment

increases with the number of elements added.

Both above mentioned aspects have stimulated efforts to create a new class of ternary Cu-base composites where the Nb is replaced by Cr and the Ag content is reduced [33]. This combination leaves room for optimizing and tailoring microstructure with respect to a particular application at costs below those required for producing conventional high-performance Cu-base composites.

2. Fundamentals of Cu–Cr and Cu–Ag alloys

Cu and Cr have small mutual solubility which decays to near zero at room temperature. Maximum solubility of Cr in Cu is 0.89 at.% (0.71 wt.%) at 1350 K. The equilibrium phase diagram of Cu and Cr reveals a Cu-rich eutectic at 1.56 at.% (1.25 wt.%) Cr and 1350 K which is characterized by the decomposition $liq \rightleftharpoons \alpha_{Cu} + \beta_{Cr}$ [38,39]. At hypereutectic compositions the shape of the Cu–Cr equilibrium phase diagram is determined by the reaction $liq \rightleftharpoons liq_{Cu} + \beta_{Cr}$. These thermodynamic boundary conditions allow one to generate four different microstructure ingredients with dissimilar mechanical and kinetic behavior, namely, primary dendritic Cr crystals in the Cu, Cr–Cu eutectic, solute Cr atoms in the Cu as well as solute Cu atoms in the Cr, and Cr precipitates formed during aging in the Cu matrix. In order to exploit these different morphologies for increasing strength the chosen alloys contained either 4.5 or 10 wt.% Cr, i.e. they were in the hypereutectic regime.

In an ordinary chill casting experiment the primary Cr crystals typically solidify with dendritic morphology. The dendrite thickness decreases with decreasing quenching time. During subsequent deformation such as swaging and wire drawing the dendrites form into fibers the spacing of which continuously drops with increasing strain. This effect renders the alloy a fiber-reinforced composite where the density of the Cu/Cr interfaces increases with increasing strain. In most Cu-bcc composites the two co-deformed phases do not undergo the same microscopic strain. The fibers typically carry less plastic deformation than the matrix. Because the mass density of Cr is 7.14 g cm⁻³ and that of Cu 8.93 g cm⁻³ gravitational segregation of the

Table 1
Compositions of the three as-cast Cu–Cr–Ag alloys

Alloy	Cr (wt.%)	Ag (wt.%)	O (ppm)	C (ppm)	Cu (wt.%)
Cu–10wt.%Cr–3wt.%Ag	10.0	3.0	128.0	11.0	Balance
Cu–10wt.%Cr–1wt.%Ag	9.6	1.0	88.8	23.4	Balance
Cu–4.5wt.%Cr–3wt.%Ag	4.5	2.7	44.8	23.5	Balance

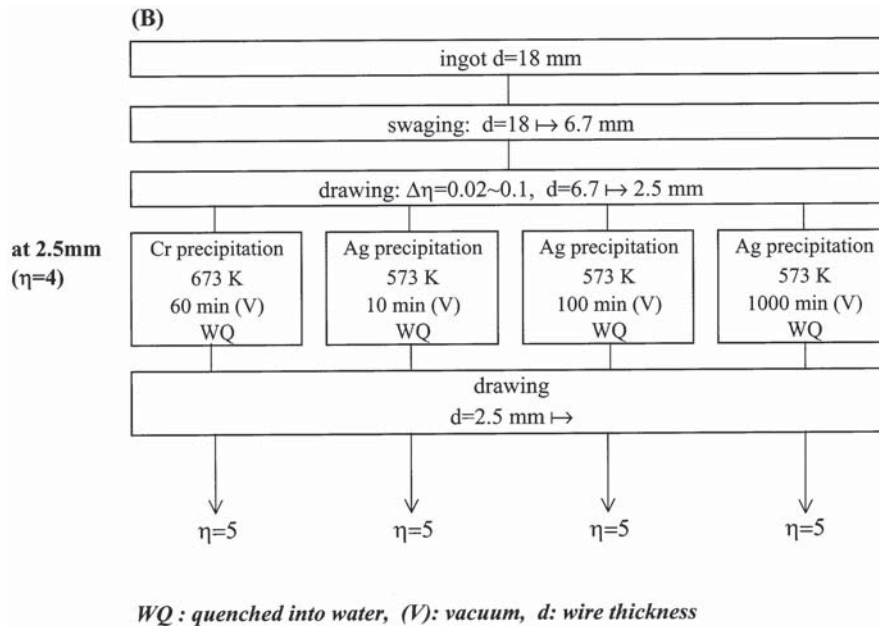
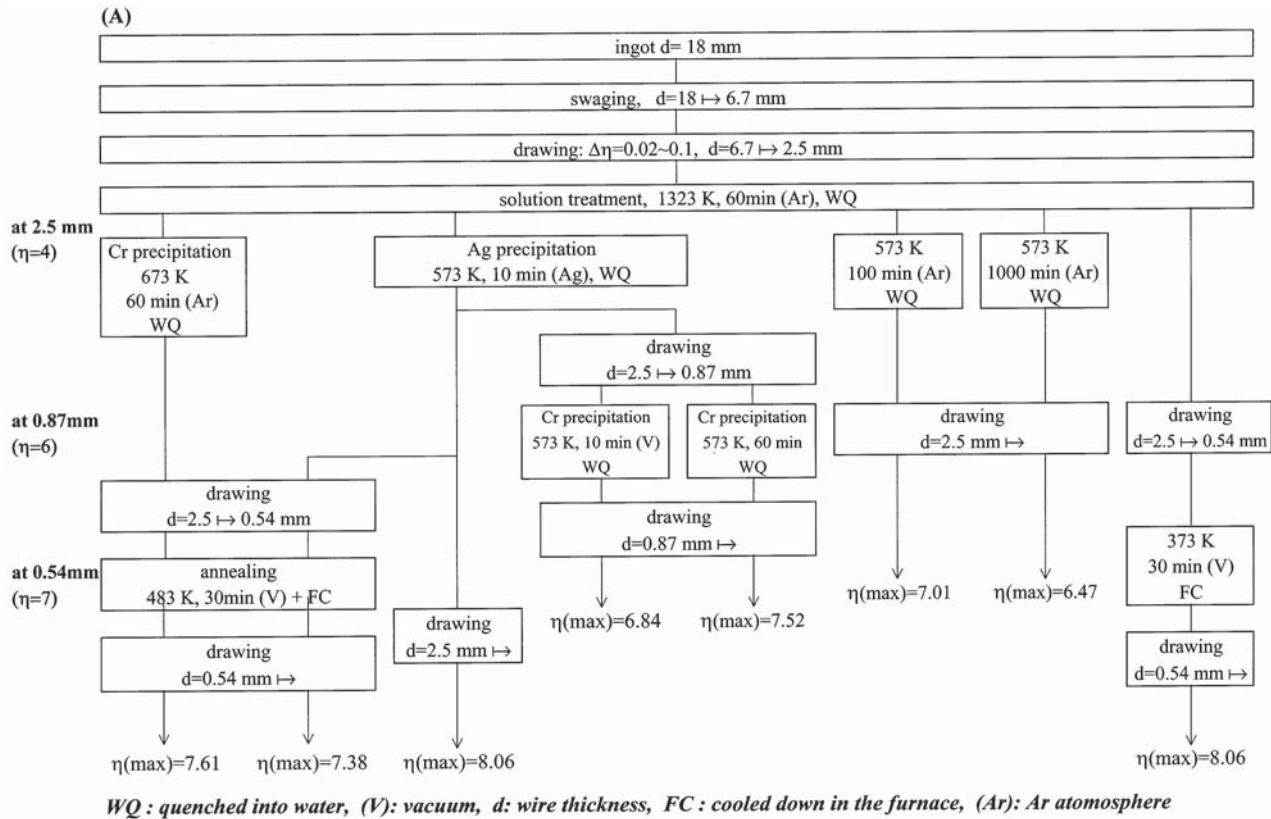


Fig. 1. (a) Processing scheme A. The various treatments are characterized by a solution temperature of 1323 K just below the temperature of maximum solubility of Cr in Cu and various subsequent aging and wire drawing schemes. (b) Processing scheme B. The various treatments are characterized by the absence of solution treatment and various aging schemes prior to further wire drawing. (c) Processing scheme C. The various treatments are characterized by a solution temperature of 1273 K, intermediate wire drawing, aging treatment at 473 K, and final wire drawing.

primary dendrites during casting is not a major concern.

Various groups studied aging of binary Cu–Cr alloys [14–16]. Ellis has investigated aging in a Cu–7vol.%Cr alloy [16]. Most of these authors agree that the ductility

of Cu–Cr alloys can be significantly enhanced by an initial or intermediate solution and subsequent aging treatment and that optimum strengthening occurs in the temperature regime between 670 and 770 K. Precipitation and ripening of Cr in Cu–Cr alloys is usually

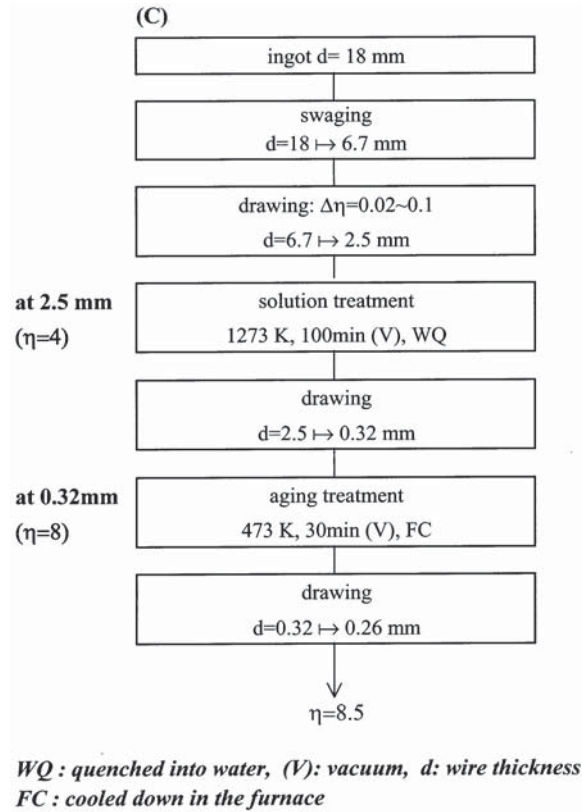


Fig. 1. (Continued)

accompanied by a drop in resistivity. Binary alloys consisting of Cu and 7 vol.% Cr were reported to reach an ultimate tensile strength (UTS) of up to 925 MPa at a total strain of $\eta = 8.5$ [15] and even up to 975 MPa at a total strain of $\eta = 9.4$ using an intermediate aging treatment [16].

Cu and Ag have limited mutual solubility. Their equilibrium phase diagram reveals a single immiscibility gap, leading to the formation of a eutectic equilibrium phase diagram with the eutectic at 60.1 at.% (72 wt.%) Ag and 1052 K which is characterized by the decomposition $\text{liq} \rightleftharpoons \alpha_{\text{Cu}} + \beta_{\text{Ag}}$ [38,39]. Maximum solubility of Ag in Cu is reported to lie between 4.2 (4.7 wt.%) and 5.2 at.% (5.8 wt.%) at 1052 K. Previous research on Cu-rich Cu–Ag composites with compositions above the maximum solubility of Ag have shown that these alloys consist of two phases, a Cu-rich solid solution and a Cu–Ag eutectic [17–24]. During deformation the eutectic and the Cu-rich matrix form into lamellar filaments where the inter-lamellar spacing decreases with wire strain. An intermediate heat treatment leads to Ag precipitation. These can be used for increasing the matrix strain and/or to form additional fibers during further drawing. At large wire strains Cu–Ag composites were reported to show an UTS of up to $\sigma = 1.5$ GPa at a strain of $\eta = 10$ [18].

As in the case of Cu–Nb and Cu–Cr composites, the observed increase in strength of Cu–Ag alloys exceeds that predicted by the linear rule of mixtures. The profile of strength and conductivity of near-eutectic Cu–Ag alloys shows a similar dependence on wire strain as Cu-bcc alloys. Recent TEM work has revealed [20], that the microstructural scale of the silver filaments in Cu–Ag is much finer than reported in earlier investigations.

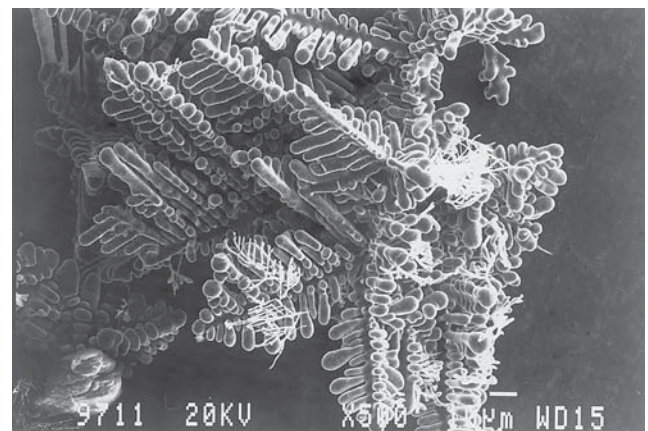


Fig. 2. SEM micrograph of the Cr microstructure of the as-cast Cu–10wt.%Cr–1wt.%Ag alloy. Cu and Ag were dissolved by selective etching.

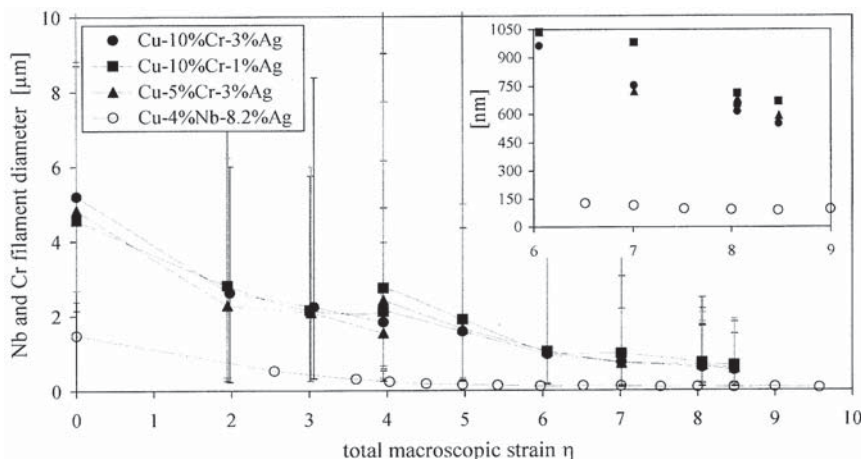


Fig. 3. Thickness of the Cr dendrites as a function of strain. The Nb data taken from Cu–4wt.%Nb–8.2wt.%Ag [33–37] are given as a reference. The large scatter is due to the fact that Cr appears in two microstructural morphologies, namely in the form of large primary dendrites with secondary and tertiary branches and in the form of thin eutectic lamellae.

When the interface spacing in the heavily deformed in situ composites is reduced to the order of the mean free electron path, the electrical conductivity of both alloy types decays with further deformation. Due to the high intrinsic conductivity of the constituents and the comparatively small contribution of inelastic interface scattering, eutectic Cu–Ag MMCs reveal, at a given strength level, a somewhat better conductivity than Cu-bcc alloys.

3. Experimental

Three compositions were chosen for the investigation, namely, Cu–10wt.%Cr–3wt.%Ag, Cu–10wt.%Cr–1wt.%Ag, and Cu–4.5wt.%Cr–3wt.%Ag. The melts were prepared using electrolytic Cu, commercial Cr with at least 99.99 wt.% purity, and commercial Ag with at least 99.9 wt.% purity. The three alloys were separately melted in a vacuum induction furnace using a magnesia crucible. The alloys were cast into a Cu mold at a temperature of ~ 1570 K. Table 1 shows the final compositions of the three as-cast alloys.

Cylindrical ingots of 18 mm diameter were cut from the as-cast samples in order to remove the oxidation layer and surface defects. From the ingots cylindrical rods were produced by rotary swaging and subsequent moderate drawing through hard metal drawing bench dies. During swaging the sample diameter was reduced from 18 to 6.7 mm. During drawing the sample diameter was further reduced from 6.7 to 2.5 mm, corresponding to an accumulated strain of $\eta 4$ ($\eta = \ln(A_0/A)$, A : wire cross-section). Starting with this microstructural state three different experimental processing schemes were used (Fig. 1a–c). Fig. 1a shows processing scheme A. It uses a solution temperature of 1323 K just below the temperature of maximum solubility of Cr

in Cu and various aging and wire drawing steps. Fig. 1b shows processing scheme B. It is characterized by the absence of solution treatment and various aging methods prior to further wire drawing. Fig. 1c shows processing scheme C. It is characterized by a solution temperature of 1273 K, intermediate wire drawing, intermediate aging treatment at 473 K, and final wire drawing. All solution and aging treatments were made under vacuum or argon atmosphere. The largest attained wire strain of $\eta = 8.48$ was realized for Cu–10wt.%Cr–3wt.%Ag specimens using processing scheme C.

Optical and scanning electron microscopy (SEM) was employed to quantitatively investigate the morphology and topology of the dendrites and fibers. For optical investigation the samples were ground and subsequently etched using a solution of 50 ml C_2H_5OH , 50

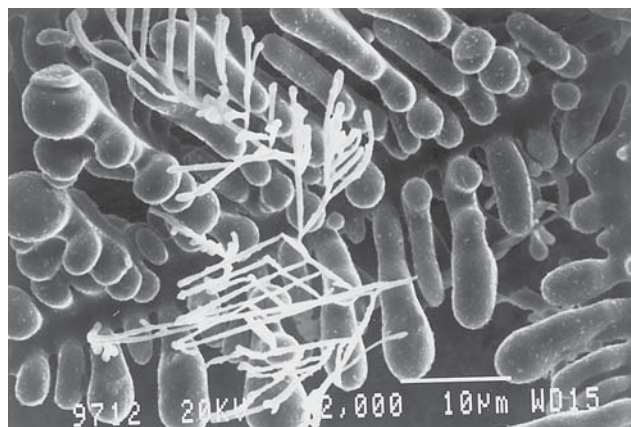


Fig. 4. SEM micrograph of Cr in the form of large primary dendrites and thin eutectic lamellae. Cu and Ag were dissolved by selective etching. The average thickness of the primary Cr dendrites in the as-cast materials is about 4500–5200 nm and that of the eutectic Cr ~ 1000 nm.

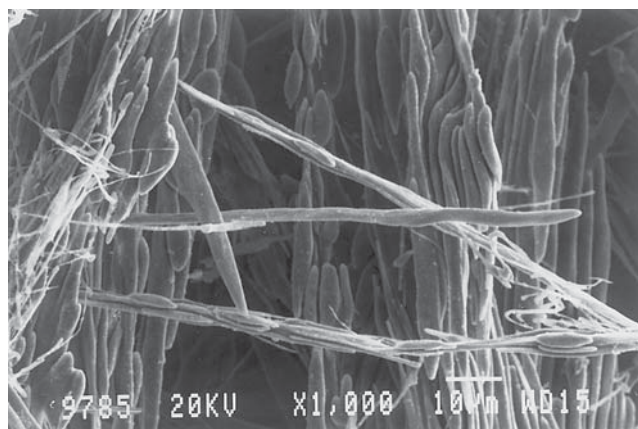


Fig. 5. SEM micrograph of the microstructures of the as-cast Cu–10wt.%Cr–1wt.%Ag alloy at a total wire strain of η_2 . Cu and Ag were dissolved by selective etching. The misalignment of some of the dendrites stems from sample preparation.

ml HF and 30 ml HNO₃. This etching removed the smeared out Cr debris which had formed during grinding on the sample surface. The filament spacing was determined by an edge-to-edge measurement. The morphology of the dendrites and fibers was measured using a selective etching technique, where the matrix was dissolved by dilute nitric acid. The mechanical properties were determined using Vickers hardness measurements with a testing mass of 200 g and tensile tests on deformed wire samples at 298 and 77 K.

4. Results and discussion

4.1. Microstructure evolution

4.1.1. As-cast specimens

Fig. 2 shows the microstructure of one of the as-cast alloys (Cu–10wt.%Cr–1wt.%Ag). In all three cases Cr had dendritic shape. The Cu matrix and the Ag were removed by selective etching prior to the SEM investigation. Due to the high quenching rate and the absence of any precipitation heat treatment directly after casting, it is likely that some Ag was still solute in the Cu-matrix. The fact that Cr solidifies with dendritic morphology can be attributed to the large temperature difference that exists in the solidification of the Cr and the Cu–Ag matrix. The average diameter of the Cr particles in the as-cast state amounted in all three alloys to $\sim d_{Cr} \approx 4500\text{--}5200$ nm. This is much larger than the average diameter of the Nb particles in Cu–4wt.%Nb–8.2wt.%Ag [33–37].

The scatter of the data given in Fig. 3 shows that the thickness distribution of the Cr dendrites is very inhomogeneous. This applies both at low and at intermediate strains. The scatter is due to the fact that Cr appears in two microstructural morphologies, namely

in the form of large primary dendrites with secondary and tertiary dendrite arms and in the form of very thin eutectic lamellae (Fig. 2). Fig. 4 shows a magnification of both types of Cr morphology in a Cu–10wt.%Cr–1wt.%Ag specimen. While the thickness of the primary Cr dendrites in the as-cast materials is close to the above-mentioned average value of 4500–5200 nm the eutectic Cr has a diameter of ~ 1000 nm.

4.1.2. Microstructure evolution during thermo-mechanical treatment

Fig. 5 presents the microstructure of the Cr dendrites after a total sample strain of $\eta_{1.98}$ for one of the three investigated alloys (Cu–10wt.%Cr–1wt.%Ag). This strain level was attained by swaging. The Cu–10wt.%Cr–3wt.%Ag and the Cu–10wt.%Cr–1wt.%Ag specimens are characterized by large and dense dendritic crystals the secondary and tertiary branches of which are aligned with the swaging axis. The misalignment of some of the elongated dendrites stems from sample preparation. Some of the very thin dendrites visible in Fig. 5 are presumably of eutectic rather than of primary dendritic origin. The Cu–5wt.%Cr–3wt.%Ag sample clearly reveals a smaller volume fraction of primary dendrites. A number of fine eutectic plates are visible as well.

Fig. 6 shows the gradual morphological evolution of the primary Cr dendrites and of the eutectic Cr dendrites into filaments. The micrographs document the shape changes observed during processing scheme C (Fig. 1c) exemplary for the Cu–10wt.%Cr–3wt.%Ag alloy. Fig. 6a reveals the microstructure at a total strain of $\eta = 3.95$ prior to the solution treatment. The dendrites appear more homogeneous than at smaller strains. However, Fig. 3 reveals very large scatter at that processing stage. Fig. 6b shows the specimen after solution treatment at 1273 K for 100 min (Fig. 1c). The elongated Cr filaments have started to coarsen, i.e. to undergo transition from fiber-type to bamboo-type morphology. In some cases the filaments even started to separate and break up into pieces. Fig. 6c gives a magnification of some filaments just before separation. Fig. 6d presents the fibers after a total strain of $\eta = 4.97$. Although the average filament thickness is still close to 2 μm some fibers reveal a thickness of only 100 nm and less. Fig. 6e shows the Cr filaments at a strain of $\eta = 8.48$, after an intermediate aging treatment and subsequent final wire drawing (Fig. 1c). The inhomogeneity of the Cr morphology observed at low and intermediate strain levels (Fig. 3) is in part a consequence of the bimodal initial size distribution of Cr (dendritic and eutectic) in the as-cast state. This heterogeneity is inherited to the later processing stages. It also shows that large deformation is necessary to produce a more homogeneous size distribution of the filaments.

A further important result in this context is the observed heterogeneous strain distribution in the investigated composites. Fig. 7 shows the total microscopic strain of the Cr filaments as a function of the total macroscopic strain of the specimens. The Cu–4wt.%Nb–8.2wt.%Ag composite which is used here as a reference [33–37] reveals a one-to-one correspondence (dotted line) at macroscopic strains below η_6 . The Cr filaments embedded in the three Cu–Cr–Ag composites reveal a one-to-two correspondence of micro- and macrostrain throughout the process. The data on Cu–

10wt.%Cr–3wt.%Ag in Fig. 7 demonstrate that this result is independent on heat treatment. This shows that solution and aging annealing — though changing the filament shape and thus influencing ductility — do not affect the intrinsic plastic properties of the Cr. Fig. 7 underlines that the Cr carries less strain than the matrix. Because the Cr has an inhomogeneous spatial distribution and undergoes an average plastic deformation much below that of the wire, the more ductile matrix phases (Cu, Ag) must undergo a higher deformation, locally. This again modifies the local stress

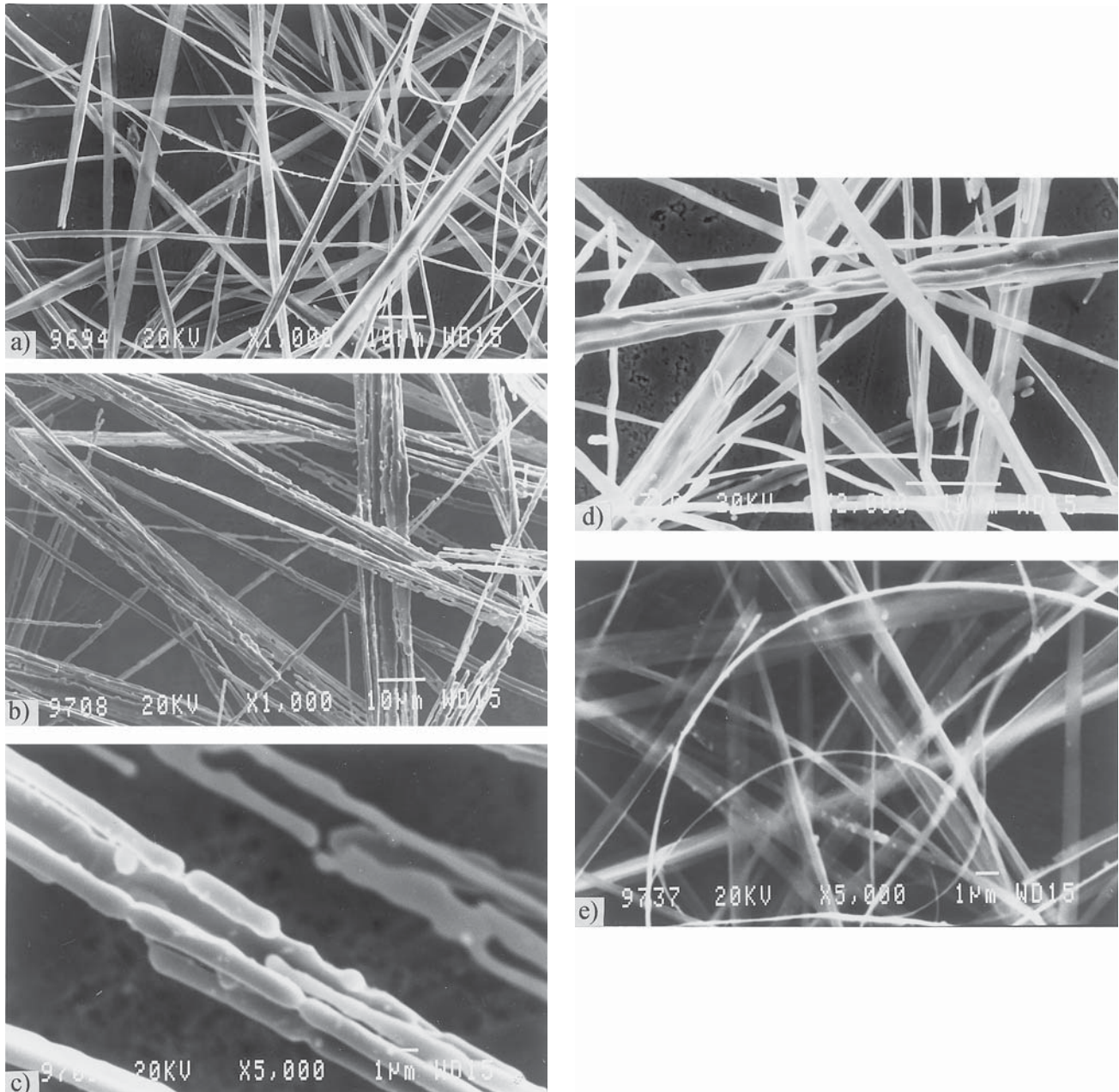


Fig. 6. SEM micrographs of the gradual evolution of the primary Cr dendrites and of the eutectic Cr lamellae into filaments; processing scheme C; Cu–10wt.%Cr–3wt.%Ag. (a) Total strain: $\eta = 3.95$; before solution treatment. (b) Total strain: $\eta = 3.95$; after solution treatment at 1273 K for 100 min. (c) Total strain: $\eta = 3.95$; after solution treatment at 1273 K for 100 min; magnification of some filaments just before separation. (d) Total strain: $\eta = 4.97$. (e) Total strain: $\eta = 8.48$; after intermediate aging treatment and subsequent final wire drawing.

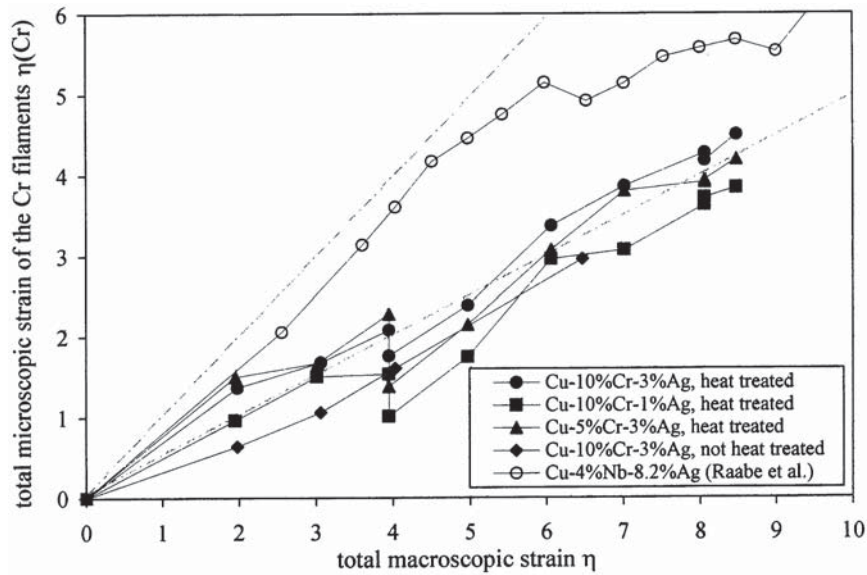


Fig. 7. Total microscopic strain of the Cr (and Nb) filaments as a function of the total macroscopic strain of the specimens. The data for Cu-4wt.%Nb-8.2wt.%Ag were taken from [33–37].

distribution within the wire, i.e. neither the actual Cu strain nor the actual Ag or Cr strain equals the true wire strain.

4.1.3. Material failure during thermo-mechanical treatment

Many of the heavily deformed specimens revealed failure during wire drawing. This applied particularly for the samples which were processed according to scheme B, i.e. without solution treatment (Fig. 1b). Fracture in these samples was characterized by conical tears which often initiated in the core of the wires (Fig. 8a,b). The micrographs suggest that fracture occurred particularly in areas with microscopical morphological instabilities. An additive and probably not-less important mechanical reason for material failure can be seen in large local stress concentrations which might arise from the unequal strain-distribution between matrix and filaments as presented in Fig. 7.

4.2. Mechanical properties and electrical conductivity

4.2.1. Hardness

Fig. 9 is an overview graph which presents the maximum obtained Vickers hardness (200 g) of Cu-10wt.%Cr-3wt.%Ag as a function of total strain for various thermo-mechanical treatments according to schemes A, B and C. The as-cast specimens had a hardness between HV 95 and HV 105. At the largest attained strain of $\eta = 8.48$ the average hardness of Cu-10wt.%Cr-3wt.%Ag reaches a value of HV 272. As is evident from group A samples (heat treatment at a strain of $\eta = 6$) and group C samples (heat treatment at a strain of $\eta = 8$) aging prior to final wire drawing sub-

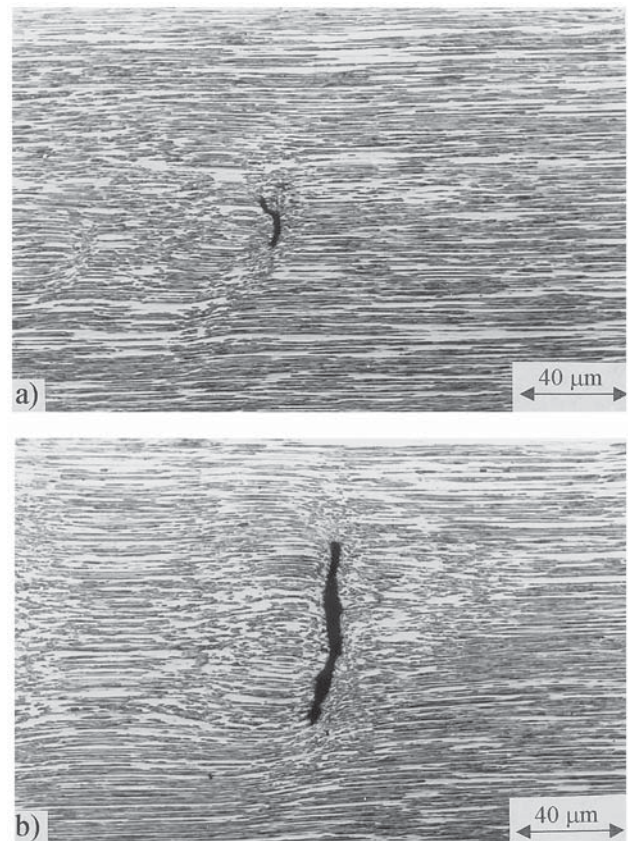


Fig. 8. (a,b) Failure during wire drawing. Fracture is characterized by conical tears which form in the core of the wires; two subsequent sketches during fracture formation; processing scheme B; Cu-10wt.%Cr-3wt.%Ag.

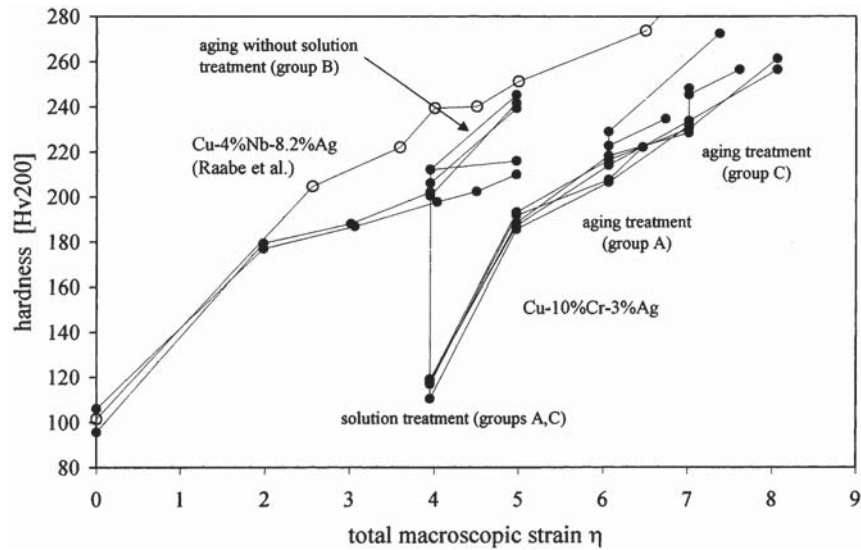


Fig. 9. Vickers hardness (200 g) of Cu–10wt.%Cr–3wt.%Ag as a function of total strain for various thermo-mechanical treatments according to schemes A, B, and C.

stantially enhances the hardness. Group B samples reveal very high hardness already at relatively small strains ($\eta=5$) much below those required by group C and group A samples for attaining the same hardness level. This effect is due to the fact that group B samples were not solution annealed and did thus not undergo softening at $\eta=4$. The absence of solution treatment entails a larger fracture tendency of group B samples so that strains beyond $\eta=5$ could not be realized (Fig. 8a,b).

Of course, increase in hardness during aging is not only a function of pre-straining but of annealing time and temperature. Fig. 9 merely summarizes the maximum values obtained for different annealing conditions. Fig. 10 exemplarily shows for group A specimens the increase in hardness as a function of annealing time at 573 K. Fig. 11 presents the time and temperature dependence of hardening attained during group C aging treatment. The diagram confirms the well-known tendency that lower aging temperatures can entail larger hardness values whilst higher aging temperatures may lead to overaging, i.e. to particle coarsening. The major advantage arising from aging after an intermediate solution treatment followed by further straining prior to aging is that larger dislocation densities provide a better distribution of potential nucleation sites. Ellis et al. reported in an investigation of a Cu–7vol.%Cr alloy [16] that Cr precipitated from solid solution during aging on the existing Cr filaments without producing a hardening effect. Due to the large strains imposed between the solution and the aging treatment it is thus conceivable that this effect was in the present case — at least to a certain extent — avoided. However, it must be taken into account that the increase in hardness as observed in the present alloys may stem from both, Cr and Ag precipitates.

4.2.2. Ultimate tensile strength

Fig. 12 shows the ultimate tensile strength of the three investigated alloys. The diagram presents data which were experimentally determined in a tensile test and compares them to data which were calculated from

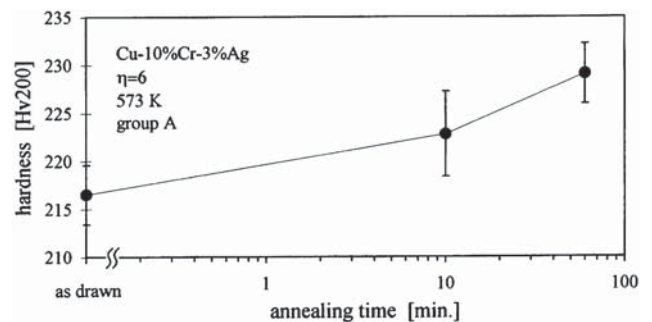


Fig. 10. Increase in hardness as a function of annealing time for a temperature of 573 K for group A samples of Cu–10wt.%Cr–3wt.%Ag at a strain of $\eta=6$.

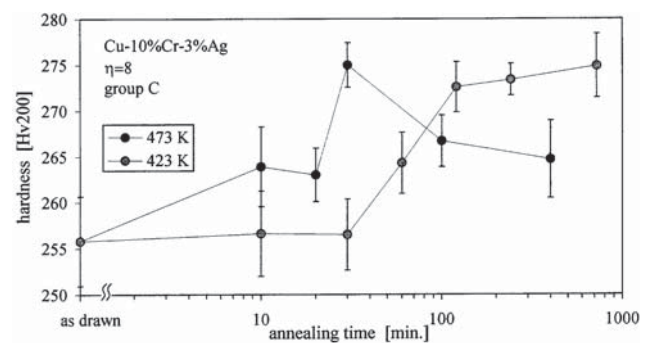


Fig. 11. Increase in hardness as a function of annealing time and annealing temperature for group C samples during aging treatment of Cu–10wt.%Cr–3wt.%Ag at a strain of $\eta=8$.

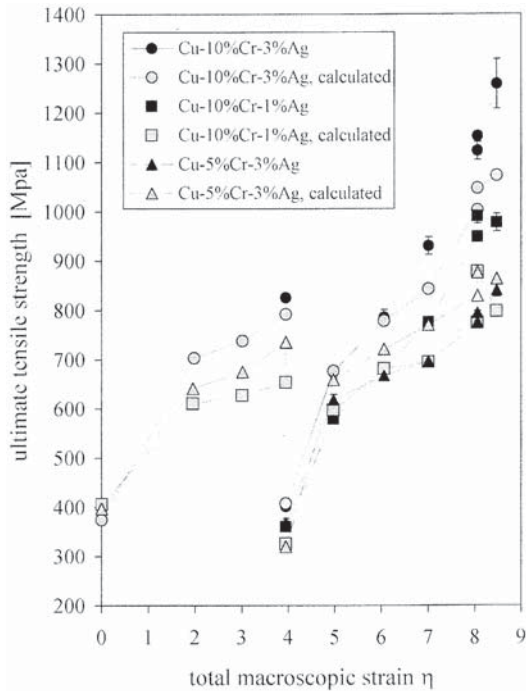


Fig. 12. Ultimate tensile strength of the three investigated alloys. The diagram presents data which were experimentally determined in a tensile test and compares them to data which were calculated from the hardness measurements.

the hardness measurements presented in the preceding section. The drop at $\eta=4$ is due to the solution treatment. The figure demonstrates that the hardness data are not sufficiently reliable for the determination of the ultimate tensile strength. The deviation between the tensile strength calculated from the hardness and the experimental tensile strength is not systematic. While the hardness data predict a strength for the Cu–4.5wt.%Cr–3wt.%Ag composite which exceeds the measured one they underestimate the strength for the other two alloys. The reason for the observed discrepancy can be explained in terms of the Vickers indentation shape which first, yields an anisotropic plastic response and second, causes a multiaxial stress state which cannot be easily translated into the stress state occurring in a tensile test carried out on a thin wire.

The ultimate tensile strength particularly of the Cu–10wt.%Cr–3wt.%Ag composite increases exponentially after the solution treatment with increasing wire strain and reaches a maximum value of 1260 MPa at $\eta = 8.48$. Fig. 13 shows a comparison of the ultimate tensile strength of Cu–10wt.%Cr–3wt.%Ag, Cu–20wt.%Nb, and Cu–4wt.%Nb–8.2wt.%Ag. The diagram substantiates that up to wire strains of $\eta \approx 8.5$ the strength is equal to that of Cu–20wt.%Nb.

4.2.3. Electrical conductivity

The use of precipitated Ag as an ingredient for hardening the Cu matrix has two aspects. First, it provides an additional Hall–Petch contribution to the overall strength of the composite. Second, the Cu–Ag interfaces have a smaller contribution to inelastic scattering of conduction electrons than the Cu–Cr interfaces. The ternary Cu–10wt.%Cr–3wt.%Ag wires reach at 300 K (total wire strain $\eta = 2.5$, after solution treat-

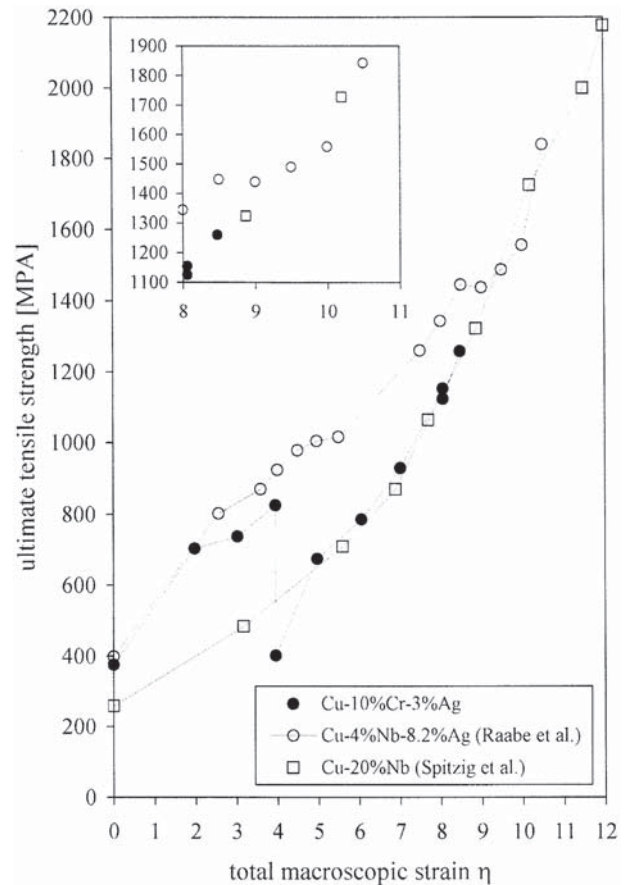


Fig. 13. Comparison of the ultimate tensile strength of Cu–10wt.%Cr–3wt.%Ag, Cu–20wt.%Nb (data taken from [10]), and Cu–4wt.%Nb–8.2wt.%Ag (data taken from [33–37]).

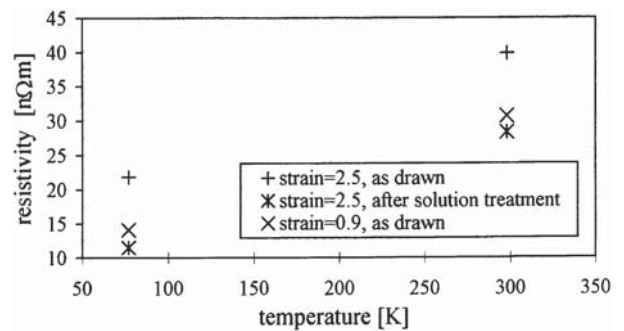


Fig. 14. Electrical resistivity of Cu–10wt.%Cr–3wt.%Ag wires at 300 and 77 K and a total wire strain of $\eta = 2.5$ before and after solution treatment.

ment) 62% of the conductivity of pure Cu (62% IACS, IACS: International Annealed Cu Standard) (Fig. 14). The drop in resistivity at 77 K is simply due to decrease of phonon scattering.

The fact that previous publications on Cu–Cr alloys [9,15] revealed higher electrical conductivity than the alloys presented here is attributed to the influence of the Ag, to the purity of the used Cr, to the thermo-mechanical processing scheme, and to the melting and casting technique. Previous authors showed [9,15] that the conductivity of Cu–Cr alloys is sensitive to the fine details of the deformation and annealing procedure, in particular to the solution and quenching methods. It is thus conceivable that the alloys shown here can be further optimized through an improved solution and precipitation procedure. The same applies to melting and casting. Cr reacts with air and the crucible material. Both effects may increase the impurity content of the Cr and deteriorate the electrical conductivity of the composite. Previous authors [9,15] have used vacuum induction and air melting under argon gas.

5. Conclusions

Three ternary in situ metal matrix composites with high strength and high electrical conductivity consisting of heavily co-deformed Cu, Cr, and Ag were introduced, namely, Cu–10wt.%Cr–3wt.%Ag, Cu–10wt.%Cr–1wt.%Ag, and Cu–4.5wt.%Cr–3wt.%Ag. The composites were produced by inductive melting, chill casting, swaging, wire deformation, and intermediate heat treatment. The main results are as follows.

(1) Cu–Cr–Ag alloys with hypereutectic Cr content are less ductile compared to previously investigated Cu–Nb, Cu–Ag, and Cu–Nb–Ag alloys.

(2) Special attention must be placed on optimizing microstructure with respect to strength, ductility, and electrical conductivity. A large number of possible thermo-mechanical processing schemes were investigated. Good results were obtained by combining pre-straining, intermediate solution treatment, intermediate wire drawing, aging treatment, and final wire drawing.

(3) Maximum ultimate tensile strength of 1260 MPa was observed for a Cu–10wt.%Cr–3wt.%Ag composite at a total wire strain of $\eta = 8.48$.

(4) The electrical conductivity of Cu–10wt.%Cr–3wt.%Ag at a total wire strain of $\eta = 2.5$ amounts to 62% of the conductivity of pure Cu (IACS).

Acknowledgements

The authors are indebted to D. Mattissen, G. Scheele, G. Gottstein and F. Heringhaus for practical

support and helpful comments. One of the authors (D.R.) gratefully acknowledges the financial support by the Deutsche Forschungsgemeinschaft through the Heisenberg program.

References

- [1] J. Bevk, J.P. Harbison, J.L. Bell, *J. Appl. Phys.* 49 (1978) 6031.
- [2] P.D. Funkenbusch, T.H. Courtney, *Acta Metall.* 33 (1985) 913.
- [3] W.A. Spitzig, A.R. Pelton, F.C. Laabs, *Acta Metall.* 35 (1987) 2427.
- [4] P.D. Funkenbusch, J.K. Lee, T.H. Courtney, *Metall. Trans. A* 18 (1987) 1249.
- [5] C. Trybus, W.A. Spitzig, *Acta Metall.* 37 (1989) 1971.
- [6] J.D. Verhoeven, W.A. Spitzig, F.A. Schmidt, P.D. Krotz, E.D. Gibson, *J. Mater. Sci.* 24 (1989) 1015.
- [7] J.D. Verhoeven, W.A. Spitzig, L.L. Jones, H.L. Downing, C.L. Trybus, E.D. Gibson, L.S. Chumbley, L.G. Fritzscheier, G.D. Schnittgrund, *J. Mater. Eng.* 12 (1990) 127.
- [8] W.A. Spitzig, *Acta Metall.* 39 (1991) 1085.
- [9] W.A. Spitzig, H.L. Downing, F.C. Laabs, E.D. Gibson, J.D. Verhoeven, *Metall. Trans. A* 24 (1993) 7.
- [10] D. Raabe, F. Heringhaus, U. Hangen, G. Gottstein, *Z. Metall.* 86 (1995) 405.
- [11] F. Heringhaus, D. Raabe, G. Gottstein, *Acta Metall.* 43 (1995) 1467.
- [12] D. Raabe, U. Hangen, *Acta Metall.* 44 (1996) 953–961.
- [13] J.T. Wood, J.D. Embury, M.F. Ashby, *Acta Mater.* 45 (1997) 1099.
- [14] C.J. Kim, J.M. Lee, *J. Mater. Process. Manuf. Sci.* 2 (1994) 325.
- [15] S.T. Kim, P.M. Berge, J.D. Verhoeven, *J. Mater. Eng. Perform.* 4 (1995) 573.
- [16] T.W. Ellis, S.T. Kim, J.D. Verhoeven, *J. Mater. Eng. Perform.* 4 (1995) 581.
- [17] H.E. Cline, D. Lee, *Acta Metall.* 18 (1970) 315.
- [18] G. Frommeyer, G. Wassermann, *Acta Metall.* 23 (1975) 1353.
- [19] S. Foner, E. Bobrov, *IEEE Trans. Magn.* 24 (1987) 1059.
- [20] S.I. Hong, M.A. Hill, *Acta Metall.* 46 (1988) 4111.
- [21] T. Asano, Y. Sakai, K. Inoue, M. Oshikiri, H. Maeda, *Japan. J. Appl. Phys.* 32 (1993) 1027.
- [22] T. Asano, Y. Sakai, M. Oshikiri, K. Inoue, H. Maeda, G. Heremans, L. van Bockstal, L. Li, F. Herlach, *IEEE Trans. Magn.* 30 (1994) 2106.
- [23] Y. Sakai, K. Inoue, H. Maeda, *Acta Metall.* 43 (1995) 1517.
- [24] Y. Sakai, H.-J. Schneider-Muntau, *Acta Metall.* 45 (1997) 1017.
- [25] H.-J. Schneider-Muntau, *IEEE Trans. Magn.* 18 (1982) 32.
- [26] F. Heringhaus, Y.M. Eyssa, P. Pernambuco-Wise, M.D. Bird, G. Gottstein, H.-J. Schneider-Muntau, *Metall* 50 (1996) 272.
- [27] J.D. Embury, M.A. Hill, W.A. Spitzig, Y. Sakai, *MRS Bull.* 8 (1993) 57.
- [28] M.A. Morris, J.C. Joyce, *Acta Metall.* 43 (1995) 69.
- [29] J. Troxel, *Adv. Mater. Proc.* 147 (1995) 35.
- [30] L.G. Fritzscheier, *Nanostruct. Mater.* 1 (1992) 257.
- [31] W.A. Spitzig, P.B. Wheelock, T.W. Ellis, F.C. Laabs, *Micromechanics of Advanced Materials*, Cleveland, OH, TMS Minerals Metals Materials Society, 1996, p. 341.
- [32] S. Spaic, M. Pristavec, *Metall* 4 (1996) 254.
- [33] D. Raabe, D. Mattissen, K. Miyake, H. Takahara, F. Heringhaus, in: P.S. Nicholson (Ed.), *Proceedings of International Conference on Dialogues at Lake Louise, Composites-Design for Performance*, Eagle Press, Burlington, Ontario, 1997, p. 146.
- [34] D. Mattissen, D. Raabe, *Metall* 51 (1997) 464.

- [35] D. Raabe, D. Mattissen, *Acta Mater.* 46 (1998) 5973.
- [36] D. Raabe, D. Mattissen, *Acta Mater.* 47 (1999) 769.
- [37] D. Mattissen, D. Raabe, F. Heringhaus, *Acta Mater.* 47 (1999) 1627.
- [38] M. Hansen, *Constitution of Binary Alloys*, McGraw–Hill, New York, 1958.
- [39] T. Massalski, *Binary Alloys Phase Diagrams*, ASM International, 1990.